

Full length article

Proton pump inhibitor-enhanced nanocatalytic ferroptosis induction for stimuli-responsive dual-modal molecular imaging guided cancer radiosensitization



Shuting Zheng^{a,b,1}, Honglei Hu^{a,b,1}, Meirong Hou^{a,b}, Kai Zhu^{a,b}, Zede Wu^{a,b}, Li Qi^d, Hui Xia^e, Guoqiang Liu^e, Yunyan Ren^a, Yikai Xu^{a,*}, Chenggong Yan^{a,*}, Bingxia Zhao^{b,c,*}

^a Department of Medical Imaging Center, Nanfang Hospital, Southern Medical University, Guangzhou 510515, PR China

^b Guangzhou Key Laboratory of Tumor Immunology Research, Cancer Research Institute, School of Basic Medical Sciences, Southern Medical University, Guangzhou 510515, PR China

^c Experiment Education/Administration Center, School of Basic Medical Science, Southern Medical University, Guangzhou 510515, PR China

^d Guangdong Provincial Key Laboratory of Medical Image Processing, School of Biomedical Engineering, Southern Medical University, Guangzhou, 510515, PR China

^e Institute of Electrical Engineering Chinese Academy of Sciences, Beijing 100190, PR China

ARTICLE INFO

Article history:

Received 12 November 2022

Revised 19 February 2023

Accepted 8 March 2023

Available online 15 March 2023

Keywords:

Proton pump inhibitor

Glucose oxidase

Ferroptosis

Fenton-like reaction

Radiosensitization

ABSTRACT

Although radiotherapeutic efficiency has been revealed to be positively correlated with ferroptosis, the neutral/alkaline cytoplasm pH value of tumor cells remains an intrinsic challenge for efficient Fenton/Fenton-like reaction-based ferroptosis induction. Herein, PEGylated hollow mesoporous organosilica nanotheranostics (HMON)-GOx@MnO₂ nanoparticles (HGMP NPs) were designed as a ferroptosis inducer, which could specifically release Mn²⁺ in tumor cells to activate the Fenton-like reaction for ferroptosis induction. Proton pump inhibitors (PPIs) were synchronously administered for cytoplasm pH level regulation by inhibiting V-H⁺-ATPases activity, enhancing Fenton-like reaction-based ferroptosis induction. Moreover, reactive oxygen species production was facilitated via the glucose oxidase triggered cascade catalytic reaction by utilizing intracellular β-D-glucose for H₂O₂ self-supply and generation of additional cytoplasm H⁺. The PPI enhanced ferroptosis inducing nanosystem effectively inhibited tumor growth both *in vitro* and *in vivo* for tumor-specific ferroptosis induction and radiotherapy sensitization, suggesting that PPI administration could be an efficient adjuvant to reinforce Fenton/Fenton-like reaction-based ferroptosis induction for radiosensitization.

Statement of significance

The cytoplasm pH value of tumor cells is typically neutral to alkaline, which is higher than that of the Fenton/Fenton-like reaction desired acidic environments, hindering its efficiency. In this study, PEGylated hollow mesoporous organosilica nanotheranostics (HMON)-GOx@MnO₂ nanoparticles were synthesized as a ferroptosis inducer, which could specifically release Mn²⁺ via depleting glutathione and then activate the Fenton-like reaction in the tumor microenvironment. The glucose oxidase was applied for H₂O₂ self-supply and addition of cytoplasm H⁺ to further boost the Fenton-like reaction. We found that proton pump inhibitors (PPIs) increased intracellular acidification by inhibiting the activity of V-H⁺-ATPases to enhance the Fenton reaction-based ferroptosis induction, suggesting PPIs administration could be a feasible strategy to reinforce ferroptosis induction for radiosensitization.

© 2023 Acta Materialia Inc. Published by Elsevier Ltd. All rights reserved.

1. Introduction

Radiotherapy (RT) is a mainstream clinical therapy for many cancers. RT does not only directly induce DNA double-strand breaks by ionizing radiation, but also generates reactive oxygen species (ROS) causing cellular damage [1,2]. Although several ef-

* Corresponding authors at: Cancer Research Institute, School of Basic Medical Sciences, Southern Medical University, No.1023-1063, South Shatai Road, Baiyun District, Guangzhou, Guangdong 510515, China.

E-mail addresses: yikaixu917@gmail.com (Y. Xu), ycgycg007@gmail.com (C. Yan), bingxiaz@gmail.com, bingxia2@foxmail.com (B. Zhao).

¹ These authors contributed equally to this work.

forts have been made to enhance RT by increasing local radiation energy or hypoxia alleviation, radioresistance remains a major issue. Recent research has reported that ferroptosis is deeply involved in the progress of RT and the therapeutic efficiency of RT can be effectively improved by increased ferroptosis [3,4]. Ferroptosis inducers, such as Erastin and RSL3, have been reported to fight against radioresistance in tumors [5]. At present, research on RT sensitization by ferroptosis induction is still in its infancy. For example, our group has successfully constructed ferroptosis-inducing nanosystems for RT sensitization through the synergistic Fenton/Fenton-like reaction and glutathione (GSH)-depletion induced inactivation of lipid hydroperoxidase glutathione peroxidase 4 (GPX4) [6,7].

It is well-known that acidic conditions are desired for the Fenton and Fenton-like reaction and the optimum pH for Fenton and Fenton-like reaction ranges from 2.0 to 5.0 [8–10]. Thus, Fenton/Fenton-like reaction-based ferroptosis induction efficiency might be improved under acidic conditions. Although an acidic extracellular microenvironment has been confirmed in solid tumors, the cytoplasm in tumor cells is typically neutral to alkaline [10,11]. A switch in cytoplasm pH value may be a new way of activating Fenton and Fenton-like reactions to augment ferroptosis induction. Vacuolar H⁺-ATPases (V-H⁺-ATPases) are important in maintaining the cellular pH gradient by pumping intracellular protons into the extracellular matrix in tumors [12,13]. Proton pump inhibitors (PPIs) belong to a class of V-H⁺-ATPases inhibitors, which have been widely used to treat digestive system diseases by blocking gastric acid secretion [14,15]. Moreover, PPIs have also been demonstrated to be effective in the manipulation of pH within intracellular organelles of tumor cells to fight against drug resistance [16,17]. However, whether the administration of PPIs contributes to enhanced Fenton/Fenton-like reaction-based ferroptosis induction remains unclear.

In addition to the cytoplasm pH value, the Fenton/Fenton-like reaction also relies on the concentration of hydrogen peroxide (H₂O₂) in the cytoplasm. Although the level of H₂O₂ in the tumor microenvironment (TME) is much higher than that in normal cells [8], abundant H₂O₂ is still preferred to reinforce ROS generation and ferroptosis induction. Glucose oxidase (GOx) has been used to generate additional H₂O₂ by the oxidation of β-D-glucose to enhance the Fenton/Fenton-like reaction [18]. More H⁺ could be supplied to further decrease cytoplasm pH value in the form of gluconic acid, which is another product of β-D-glucose oxidation [19]. Benefiting from the synergistic H₂O₂ self-supply and generation of additional H⁺ mediated by gluconic acid, GOx would perform well in promoting the efficacy of ferroptosis induction.

To verify the function of PPIs and GOx in the Fenton/Fenton-like reaction enhanced ferroptosis induction, TME-activated PEGylated hollow mesoporous organosilica nanotheranostics (HMON)-GOx@MnO₂ nanoparticles (HGMP NPs) were constructed as a nanocatalytic ferroptosis inducer in this study, as emerging studies have reported that manganese dioxide (MnO₂) is a promising chemodynamic agent for ferroptosis induction via the manganese ion (Mn²⁺)-mediated Fenton-like reaction to produce ROS [20,21]. Moreover, intracellular overexpressed glutathione (GSH) could be depleted via the redox reaction by the MnO₂/disulfide bond in the HMON core. This strategy not only increased GSH-mediated elimination of ROS generated by the Fenton/Fenton-like reaction, but also inhibited the activity of GSH-dependent GPX4. The inactivation of GPX4 could further accelerate ferroptosis induction through weakened lipid peroxides detoxification [22–24]. PPIs were administrated to regulate cytoplasm pH level by inhibiting the activity of V-H⁺-ATPases to synergistically boost the Fenton-like reaction mediated by HGMP NPs. Moreover, GOx has the potential to trigger a cascade catalytic reaction by utilizing intracellular β-D-glucose for an additional supply of H₂O₂ and H⁺. This Fenton-like reaction

based ferroptosis inducing nanosystem was then applied to sensitize RT for cancer therapy. Moreover, the HGMP NPs may be utilized for T1-weighted MR imaging due to the favorable T1 relaxivity of released Mn²⁺ [25,26] and photoacoustic (PA) imaging to monitor the distribution of NPs in the tumor area. In brief, PPI administration could be a promising strategy to enhance ferroptosis induction of HGMP NPs to achieve efficient cancer RT. The mechanism of PPI-enhanced Fenton reaction-based ferroptosis induction for radiosensitization is illustrated in Scheme 1.

2. Materials and methods

2.1. Materials

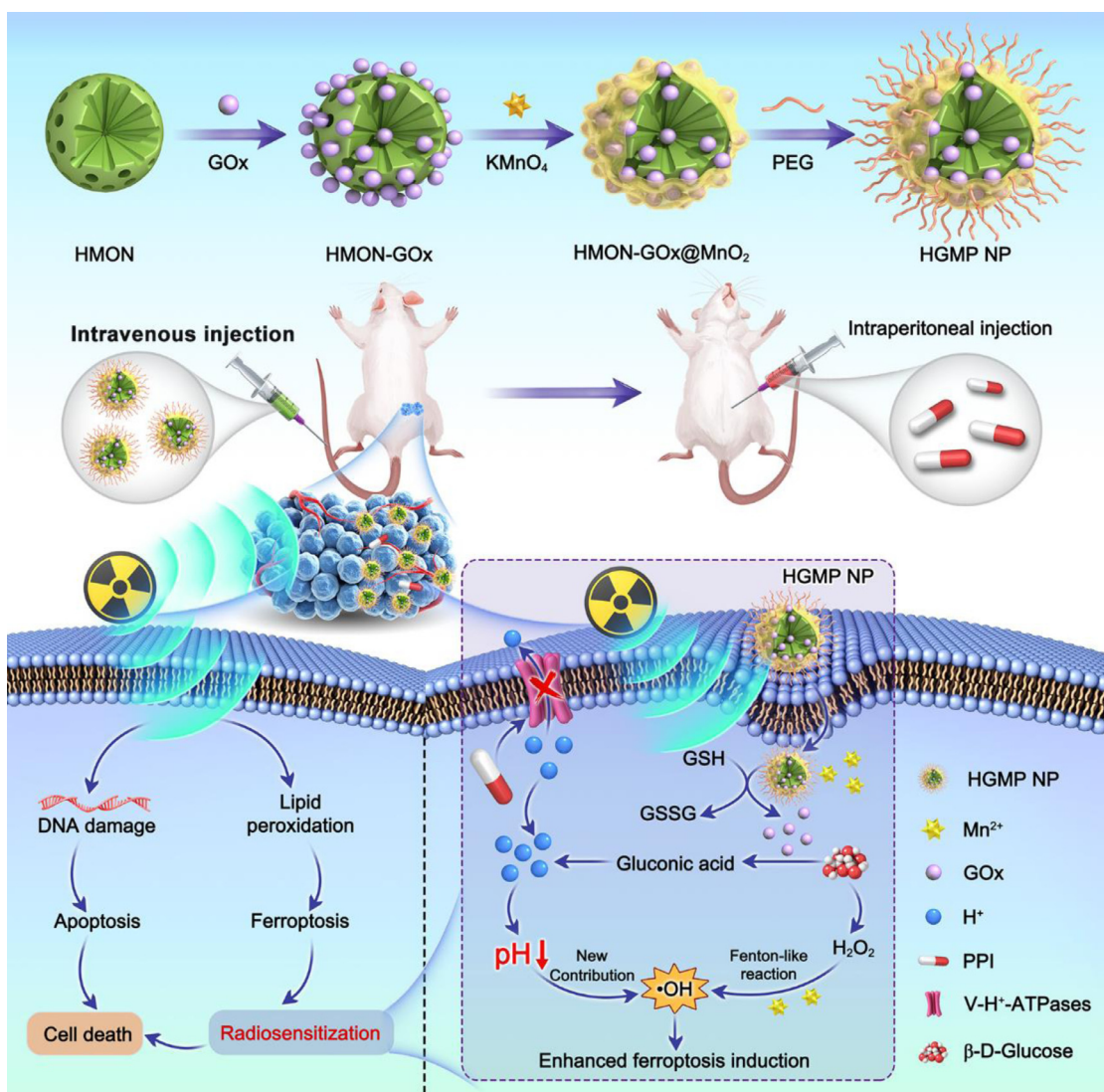
Triethanolamine (TEA), tetraethyl orthosilicate (TEOS), N-hydroxysuccinimide (NHS), Glucose oxidase (GOx), Omeprazole, methylene blue (MB), D-Gluconic acid solution (49–53 wt%), β-D-Glucopyranose, DSPE-MPEG2000, and Ferrostatin-1 (Fer-1) were purchased from Macklin, Shanghai, China. (3-aminopropyl) triethoxysilane (APTES), cetyltrimethylammonium chloride solution (CTAC), ammonia aqueous solution (NH₃·H₂O, 25 wt%) and sodium bicarbonate (NaHCO₃) were obtained from Sigma-Aldrich, USA. Bis [3-(triethoxysilyl) propyl] tetrasulfide (BTES), 1-(3-diaminopropyl)-3-ethylcarbodiimide hydrochloride (EDC), hydrogen peroxide solution (H₂O₂, 30%) and reduced-glutathione were purchased from Aladdin, Shanghai, China. Trichloromethane (CH₃Cl₃), hydrochloric acid (HCl, 37%) and Potassium permanganate (KMnO₄) were purchased from Chemical Reagent Factory, Guangzhou, China. L-buthionine sulfoximine (L-BSO) was from Selleck, China. Dichlorofluorescein diacetate (DCFH-DA) was acquired from Meilun Biotech, Dalian, China. BODIPY 581/591 C11 was purchased from Invitrogen, USA. 2',7'-bis-(2-carboxyethyl)-5-(and-6)-carboxyfluorescein, acetoxyethyl ester (BCECF AM) was from Beyotime, Shanghai, China. The Cell Counting Kit-8 (CCK-8) assay was from Dojindo, Tokyo, Japan. RPMI-1640 medium, Minimum essential medium alpha (MEM alpha), fetal bovine serum (FBS), Penicillin-Streptomycin and 0.05% trypsin-EDTA were purchased from Gibco, Thermo Fisher, USA.

2.2. Cell lines and animals

The MC3T3-E1 cells were donated by the Research Center of Clinical Medicine, Nanfang Hospital (Guangzhou, China). The mouse breast cancer cell line 4T1 was provided by Procell Life Science & Technology Co., Ltd. which was a stock cell line passed by FuDan IBS Cell Center. Use of the cell line was approved by our institutional Laboratory Animal Management Committee. The 4T1 cells were cultured in RPMI-1640 medium, while MC3T3-E1 cells were seeded in MEM-alpha medium containing 10% FBS, 100 units/mL of penicillin and 100 µg mL⁻¹ of streptomycin. Cells were incubated in a humidified atmosphere of 5% CO₂, 1% O₂, and 94% N₂ at 37°C. Female Balb/c mice (~5 weeks) were purchased from Southern Medical University Laboratory Animal Center (Guangzhou, China). All animal experimental procedures were approved by the Experimental Animal Ethics Committee of Nanfang Hospital.

2.3. Synthesis of HMON

A total of 2.1 mL CTAC solution and 50 µL TEA solution were added to 20 mL water. After heating to 95°C, 1 mL of TEOS was added dropwise into the mixed solution and stirred for 1 h. A mixture of BTES (1 mL) and TEOS (1 mL) was then added and reacted for another 4 h. MSNs were obtained by centrifugation (10,000 rpm, 10 min) and washed with ethanol three times. Subsequently, the products were dispersed in 30 mL ddH₂O containing 8.4 mL



Scheme 1. Scheme illustration of PPI administration for cytoplasm pH level regulation to promote the Fenton-like reaction based ferroptosis inducing nanosystem (HGMP NPs) for sensitizing radiotherapy. Ionizing radiation directly generated DNA double-strand breaks and lipid peroxidation, leading to apoptosis and ferroptosis. Ferroptosis inducing nanosystem, HGMP NPs, depleted intracellular GSH and generated Mn²⁺ to activate Fenton-like reaction for ROS generation. Meanwhile, the released GOx further enhanced the efficiency of Fenton-like reaction by catalyzing β-D-glucose oxidation into H₂O₂ and gluconic acid. In addition, PPI was administrated to regulate cytoplasm pH level by inhibiting the V-H⁺-ATPases activity to synergistically promote the Fenton-like reaction-based ferroptosis induction for sensitizing RT.

HCl solution (37%) and reacted at 80°C for 12 h to remove the residual CTAC, then washed with ethanol, and the same procedure was repeated twice. Finally, the HMN NPs were obtained by the ammonia solution-mediated etching reaction at 60°C for 3 h. The obtained HMN NPs were suspended in ddH₂O after centrifugation and washed with water.

2.4. Synthesis of HMN-GOx

Firstly, 10 mg of HMN were dissolved in 20 mL ethanol solution. Ammonia aqueous solution (400 μL) and APTES (60 μL) were added in turn. After reacting for 4 h, the products HMN-NH₂ were obtained by centrifugation (10,000 rpm, 10 min), washed with water, and then dispersed in 10 mL water. Subsequently, to activate the carboxyl groups of GOx, EDC (40 mg), NHS (32 mg) and GOx (10 mg) were dissolved in 10 mL of ddH₂O and stirred for 30 min in the dark. Subsequently, 10 mL of HMN-NH₂ aqueous solution (1 mg mL⁻¹) was added to the mixture under stirring overnight. Finally, the mixture was centrifuged (12,000 rpm, 5 min) and washed with water to acquire HMN-GOx.

2.5. Synthesis of PEGylated HMN-GOx@MnO₂

A total of 10 mL of HMN-GOx solution (1 mg mL⁻¹) was added dropwise into KMnO₄ solution (10 mL, 2 mg mL⁻¹) and then stirred for 30 min. The collected HMN-GOx@MnO₂ were washed and suspended in water. In order to improve the biocompatibility and water-solubility, HMN-GOx@MnO₂ (1 mg) and DSPE-mPEG (5 mg) were dissolved in chloroform and stirred for 24 h. Subsequently, PEGylated HMN-GOx@MnO₂ were obtained by centrifugation and resuspended in ddH₂O.

2.6. Characterization

Transmission electron microscopy (TEM) images and high-angle annular dark-field (HADDF)-scanning transmission electron microscopy (STEM)-based elemental mapping images were required by a JEOL JEM-2100F TEM. The UV-Vis absorption spectra were recorded on an UV-2600 UV-vis spectrophotometer from Shimadzu, Japan. The zeta potential of samples was examined by a Zetasizer Nano ZS (Malvern). Determination of silicon and manganese

contents was measured by an Inductively Coupled Plasma Optical Emission Spectrometer (ICP-OES). MR imaging was obtained with a 3.0 T Ingenia MRI scanner. PA imaging was obtained using the multispectral optoacoustic tomography system (iThera Medical GmbH, Neuherberg, Germany).

2.7. Detection of gluconic acid

Firstly, β -D-glucose (4.5 mg mL^{-1}) was added to the NPs (1 mg mL^{-1}) or GSH (10 mM), and then the mixtures were kept at 37°C for 6 and 12 h, respectively. Subsequently, the supernatant (1.6 mL) was obtained by centrifugation, then $500 \mu\text{L}$ of the mixed solution with EDTA (5 mM) and trimethylamine (0.15 mM) was added to the supernatant, followed by $50 \mu\text{L}$ of hydroxylamine (3 M). The solution was left to stand at 37°C for 25 min. Finally, the solution was mixed with $250 \mu\text{L}$ of a mixture of HCl (1 M), iron chloride hexahydrate (0.06 M) and trichloroacetic acid (0.25 M). The absorbance change at 400–700 nm was directly measured using a UV-vis spectrophotometer.

2.8. Detection of H_2O_2

The β -D-glucose (4.5 mg mL^{-1}) was added to different NPs (1 mg mL^{-1}) solutions containing GSH (10 mM), and then the mixtures were kept at 37°C . Then at pre-determined time points (0.5, 1, 2, 3 and 4 h), the supernatant was obtained by centrifugation and the content of H_2O_2 was measured using Micro H_2O_2 Assay Kit (Solarbio, Beijing, China).

2.9. GSH depletion assessment

The GSH (1 mM) was added into pure water, HMP NPs solution, and HGMP NPs solution ([Mn]: 0.5 mM) containing β -D-glucose (4.5 mg mL^{-1}), respectively. After incubation at 37°C for 1 h, the content of GSH in various different solutions was measured using Reduced Glutathione (GSH) Content Assay Kit (Solarbio, Beijing, China).

2.10. Detection of ROS

Methylene blue (MB) was used to assess the ROS generation of HMP NPs or HGMP NPs. The NPs ([Mn]: 0.5 mM) were added to 1 mL of PBS (pH 7.4 or 6.5) containing NaHCO_3 (25 mM), GSH (0, 0.5, 1, 4, 8 or 10 mM), H_2O_2 (0, 1.25, 2.5, 5 or 10 mM), glucose (4.5 mg mL^{-1}), and MB ($10 \mu\text{g mL}^{-1}$). After incubation at 37°C for 30 min, the absorbance change of MB degradation was recorded at 550–750 nm.

2.11. In vitro cell cytotoxicity assay

The 4T1 cells (8,000 cells/well) and MC3T3-E1 cells (8,000 cells/well) were seeded in a 96-well plate. After overnight incubation, PPI was added to the HGMP + PPI-treated group. After 12 h PPI pretreatment, the medium containing various concentrations of substances (PBS, HMP, HGMP) was added and then incubated for another 24 h. Subsequently, cell viability was evaluated by the CCK-8 assay. Similarly, 4T1 cells were seeded in a 96-well plate, and then treated with fresh medium containing Fer-1 (10 μM) or L-BSO (100 μM). After 6 h pretreatment, 4T1 cells were further incubated with HGM NPs ([Mn]: 4.5 mg mL^{-1}) for another 24 h. Lastly, cell viability was evaluated by the CCK-8 assay.

2.12. In vitro uptake of HGMP NPs

HGMP NPs were modified with FITC and incubated with 4T1 cells. Then at pre-determined time points (0, 1, 2, 4 and 8 h), the fluorescent intensity in 4T1 cells was analyzed by flow cytometry.

2.13. Intracellular pH analysis

BCECF AM, a pH fluorescent probe, was used to evaluate the cellular pH level. Firstly, 4T1 cells were seeded in a 6-well plate. After cells attached to the plate, fresh medium containing various substances was added: (1) PBS; (2) PPI ($25 \mu\text{g mL}^{-1}$); (3) HMP ([Mn]: $4.5 \mu\text{g mL}^{-1}$); (4) HGMP ([Mn]: $4.5 \mu\text{g mL}^{-1}$) and (5) HGMP ([Mn]: $4.5 \mu\text{g mL}^{-1}$) + PPI pretreatment ($25 \mu\text{g mL}^{-1}$) for 6 h, respectively. Subsequently, the medium in each well was replaced with serum-free medium containing BCECF AM (5 μM). After incubation for 30 min, the stained cells were observed with a fluorescent microscope.

2.14. Intracellular H_2O_2 and GSH content analysis

To analyze the intracellular GSH, 4T1 cells were seeded in a 6-well plate and treated with (1) PBS, (2) HMP ([Mn]: $2.25 \mu\text{g mL}^{-1}$), (3) HGMP, (4) HGMP + PPI, respectively. After incubation of 12 h, the GSH content in 4T1 cells was analyzed using Reduced Glutathione (GSH) Content Assay Kit (Solarbio, Beijing, China).

To analyze the intracellular H_2O_2 , 4T1 cells were seeded in a 6-well plate and treated with (1) PBS, (2) HMP ([Mn]: $2.25 \mu\text{g mL}^{-1}$), (3) HGMP, (4) HGMP + PPI, respectively. After incubation of 12 h, H_2O_2 content in 4T1 cells was evaluated using Micro H_2O_2 Assay Kit (Solarbio, Beijing, China).

2.15. Intracellular ROS analysis

The 4T1 cells were seeded in a 6-well plate and treated with (1) PBS; (2) HMP ([Mn]: $4.5 \mu\text{g mL}^{-1}$); (3) HGMP ([Mn]: $4.5 \mu\text{g mL}^{-1}$) and (4) HGMP ([Mn]: $4.5 \mu\text{g mL}^{-1}$) + PPI ($25 \mu\text{g mL}^{-1}$, 12 h pretreatment) for 6 h. After washing with PBS buffer, the DCFH-DA was added into each well for 30 min in the dark. Subsequently, the fluorescence images were captured by a fluorescent microscope (Nikon Eclipse T1-U, Tokyo, Japan). ROS levels were further analyzed by flow cytometry (BD LSRIFortessaTM Cell Analyzer, USA).

2.16. Intracellular lipid peroxidation detection

Intracellular lipid peroxidation levels were assessed by the lipid peroxidation probe BODIPY 581/581 C11. Briefly, 4T1 cells were seeded in a 6-well plate and treated with (1) PBS; (2) HMP ([Mn]: $4.5 \mu\text{g mL}^{-1}$); (3) HGMP ([Mn]: $4.5 \mu\text{g mL}^{-1}$) and (4) PPI pretreatment ($25 \mu\text{g mL}^{-1}$, 12 h) + HGMP ([Mn]: $4.5 \mu\text{g mL}^{-1}$) for 24 h. The cells were then stained with BODIPY 581/581 C11 for 1 h in the dark and analyzed by flow cytometry. After staining, the cells were observed with a fluorescent microscope.

2.17. Western blot analysis

The V-H⁺-ATPases, GPX4, and PTGS2 protein expression were analyzed by western blot. 4T1 cells were seeded in a 6-well plate at 37°C overnight, and then incubated with different concentrations of PPI for another 24 h. Subsequently, the collected cell lysates were examined by polyacrylamide gel electrophoresis to evaluate V-H⁺-ATPases protein expression. Similarly, cell lysates from the HMP ([Mn]: $4.5 \mu\text{g mL}^{-1}$), HGMP ([Mn]: $\mu\text{g mL}^{-1}$), or PPI pretreatment + HGMP ([Mn]: $\mu\text{g mL}^{-1}$) groups were collected after 24 h treatment to evaluate the expression of GPX4 or PTGS2 protein.

2.18. Intracellular clonogenic assay and immunofluorescence analysis of γ -H2AX

The 4T1 cells were seeded in a 6-well plate for 24 h, and treated with (1) PBS, (2) HMP ([Mn]: $2.25 \mu\text{g mL}^{-1}$), (3) HGMP

([Mn]: $2.25 \mu\text{g mL}^{-1}$) and (4) PPI pretreatment ($25 \mu\text{g mL}^{-1}$, 12 h) plus HGMP ([Mn]: $2.25 \mu\text{g mL}^{-1}$), respectively. Following incubation for 6 h, cells were exposed to 0, 2, 4 and 6 Gy X-ray radiation (MultiRad Faxitron, USA), respectively. The cells were then incubated for another 7 days. Lastly, the cells were fixed with paraformaldehyde followed by crystal violet staining. The survival fraction was used to evaluate the effect of various treatment on the cells.

For immunofluorescence analysis of γ -H2AX, 4T1 cells were seeded in CLSM dishes and cultured overnight. The cells were then treated as mentioned above. Following incubation for 24 h, the cells were stained using the DNA damage Assay Kit by γ -H2AX Immunofluorescence (Beyotime, Shanghai, China) to detect cell DNA damage. Images were captured by CLSM.

2.19. Immunogenic death evaluation

For the immunofluorescence analysis of CRT exposure and the release of HMGB1, 4T1 cells were seeded into confocal dishes and cultured overnight. Then treated with (1) PBS, (2) HGMP ([Mn]: $2.25 \mu\text{g mL}^{-1}$), (3) RT (4 Gy) and HGMP + RT, respectively. Following incubation for 24 h, the cells were fixed, permeabilized and incubated with CRT and HMGB1 antibodies, respectively. After overnight, the cells were incubated with FITC-labeled secondary antibodies and finally stained with DAPI. The images were acquired by CLSM.

For the analysis of ATP production *in vitro*, 4T1 cells were seeded in a 6-well plate and treated with (1) PBS, (2) HGMP ([Mn]: $2.25 \mu\text{g mL}^{-1}$), (3) RT (4 Gy) and HGMP + RT, respectively. After incubation of 24 h, ATP in 4T1 cells was assessed using ATP Assay Kit (Beyotime, Shanghai, China).

2.20. In vitro and in vivo PA imaging assessment

The HGMP aqueous solutions at different Mn concentrations (0, 0.1, 0.2, 0.4, 0.8 mM) were scanned at different wavelengths by the multispectral optoacoustic tomography system. The slope was calculated using the fitting curve of average PA signal intensity and NPs concentration. 4T1 tumor-bearing mice were intravenously injected with HGMP solutions ([Mn]: 4 mg kg^{-1}) or saline, and then subjected to PA imaging at a wavelength of 680 nm at predetermined intervals (0, 3, 6 and 12 h post-injection).

2.21. In vitro and in vivo MRI assessment

The HGMP aqueous solutions at different concentrations of Mn (0, 0.05, 0.1, 0.2 or 0.4 mM) were incubated in 1 mL of PBS with or without GSH (10 mM). After 10 min, the solutions were scanned using a 3.0 T Ingenia MRI scanner (Philips, Amsterdam, Netherlands). Subsequently, HGMP solutions ([Mn]: 4 mg kg^{-1}) were intravenously injected into 4T1 tumor-bearing mice, and then MR images were obtained using the T1-weighted sequence (TR = 450.0 ms, TE = 15.3 ms, thickness = 2 mm) at predetermined intervals to evaluate the contrast enhancement of NPs *in vivo*.

2.22. The biodistribution and quantitative analysis of HGMP NPs

The 4T1 tumor-bearing mice were intravenously injected with HGMP NPs (2 mg kg^{-1}) in saline when the tumor volume grew to around $50\text{--}80 \text{ mm}^3$. Then at pre-determined time points (3, 6, 12, 24, and 48 h) of post-injection ($n = 3$), the mice were sacrificed and the Mn contents in the tumor quantified by ICP-MS (NexION 2000).

2.23. *In vivo* antitumor effect

The 4T1 tumor-bearing mice were randomly divided into 8 groups ($n = 4$ in each group): (1) saline, (2) HMP NPs; (3) HGMP NPs; (4) HGMP NPs + PPI; (5) RT; (6) HMP NPs + RT; (7) HGMP NPs + RT; (8) HGMP NPs + PPI + RT. The NPs ([Mn]: 2 mg kg^{-1}) were intravenously injected into each tumor-bearing mouse. Then tumors in the RT treated groups received X-ray radiation (6 Gy) at 6 h post-injection. PPI (100 mg kg^{-1}) was given by intraperitoneal injection every 3 days for three cycles. The tumor volume and body weight of mice were measured every 2 days. The tumor volume was calculated by length \times width $^2 / 2$, and the relative tumor volume was estimated by dividing by the initial tumor volume pre-treatment. After 14 days, all mice were euthanized and their tumor tissues were excised and fixed in 4% formalin for histopathological analyses with H&E staining and immunohistochemistry (TUNEL, γ -H2AX, GPX4 and 4-HNE). Additionally, blood from the PBS group and the group treated with HGMP for 14 days was collected for biochemical analysis.

2.24. The evaluation of pH value in tumor site

A dose of PPI (100 mg kg^{-1}) in saline was intraperitoneally injected into 4T1 tumor-bearing mice. Subsequently, the mice were injected with a pH probe SNARF-1 ($10 \mu\text{M}$) in saline at pre-determined time points. After 20 min, mice were sacrificed and the tumor tissues were collected for imaging. *Ex vivo* fluorescent images of tumor tissue were acquired under the IVIS Lumina System (IVIS Lumina II, USA) at 500–550 nm.

2.25. The evaluation of ROS in tumor site

Dihydroethidium (DHE) was used as a probe to detect ROS generation in tumor site. The 4T1 tumor-bearing mice were randomly divided into 8 group: (1) saline, (2) HMP NPs; (3) HGMP NPs; (4) HGMP NPs + PPI; (5) RT; (6) HMP NPs + RT; (7) HGMP NPs + RT; (8) HGMP NPs + PPI + RT. Firstly, the NPs ([Mn]: 2 mg kg^{-1}) were intravenously injected into each tumor-bearing mouse and PPI (100 mg kg^{-1}) was given by intraperitoneal injection. Then tumors in the RT treated groups received X-ray radiation (6 Gy) at 6 h post-injection. After 2 h, all mice were euthanized and their tumor tissues were excised for immunohistochemistry.

2.26. *In vivo* biosafety evaluation

To evaluate the biosafety of HGMP and PPI administration, the main organs (heart, lung, liver, spleen, and kidney) from the PBS, PPI and HGMP + PPI groups were collected on the 7 days after treatment, respectively. Subsequently, the above tissues were stained with H&E. Meanwhile, the blood was obtained for a series of measurements such as blood biochemical indexes.

2.27. Statistical analysis

All data are expressed as the mean \pm standard deviation (SD). The Student t test or Analysis of Variance (ANOVA) was used to analyze the differences using Prism 8.0 software (GraphPad Software). P-values less than 0.05 were considered statistically significant. All experiments were repeated at least three times.

3. Results and discussion

3.1. Synthesis and characterization of HGMP NPs

The HMN was synthesized according to a previously reported method [27]. GOx was bonded to amino-modified HMN

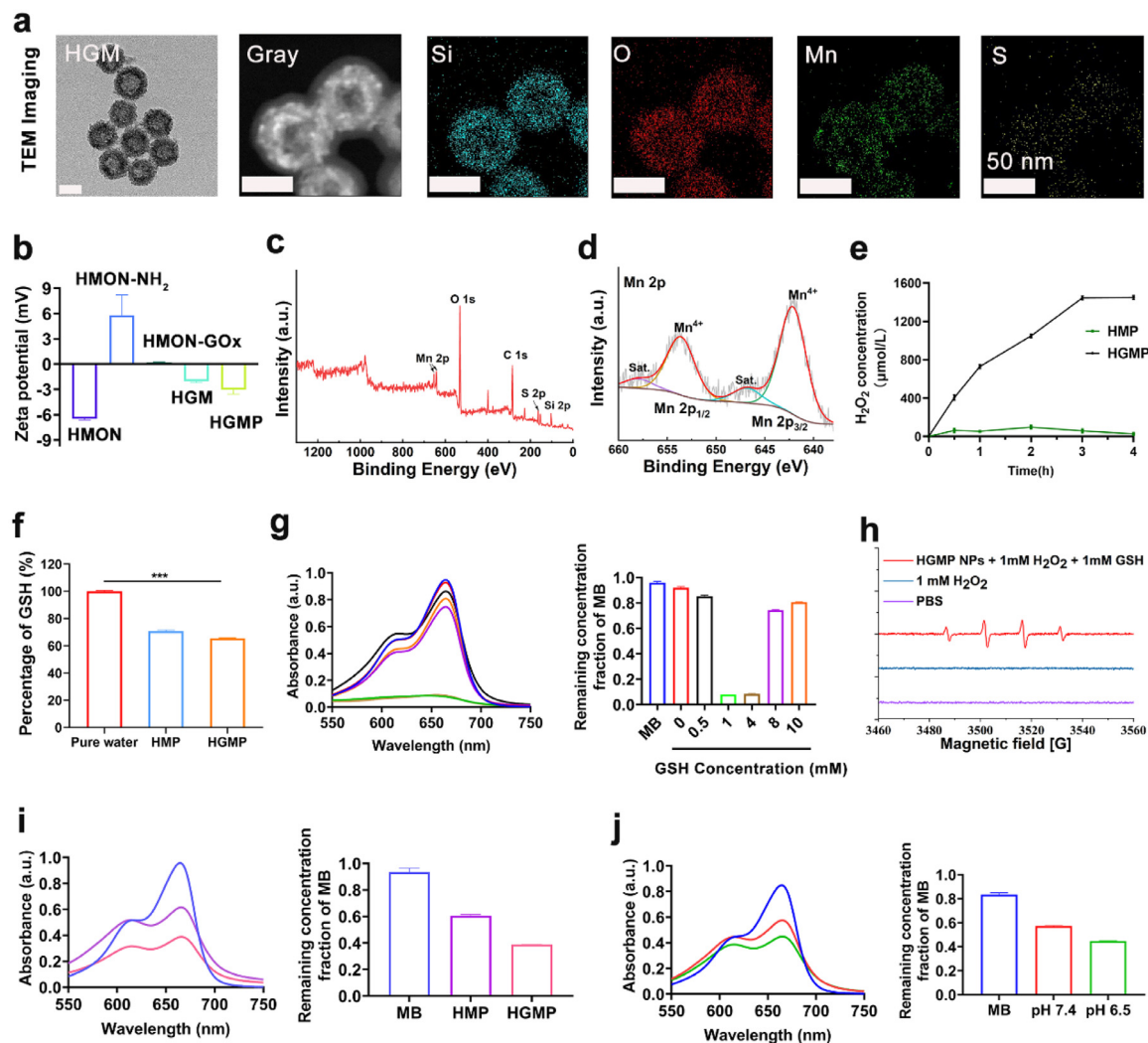


Fig. 1. Characterization of HGMP NPs. (a) The TEM images of HGM NPs and element mapping images of Si, O, Mn and S for HGM NPs. (b) The zeta potential change of each step in the synthetic process of HGMP NPs. Data were presented as mean \pm SD ($n = 3$ for each group). (c) XPS image of HGMP NPs. (d) High-resolution XPS spectra of Mn 2p of HGMP NPs. (e) The generated H₂O₂ concentration in different NPs solutions after incubation with glucose at predetermined time points. (f) The relative GSH concentration in different solutions with glucose. Data were presented as mean \pm SD ($n = 3$ for each group). (g) The UV-vis absorption spectra of MB degradation in HMP NPs solutions with the existence of H₂O₂ (10 mM) and different concentration of GSH, and their relative quantification of MB at 665 nm. Data were presented as mean \pm SD ($n = 3$ for each group). (h) ESR spectra of various solutions. (i) The UV-vis absorption spectra of MB degradation in HMP NPs solutions and HGMP NPs solutions under the same conditions ([Mn]: 0.5 mM, GSH: 4 mM, H₂O₂: 1 mM, glucose: 4.5 mg mL⁻¹) and their relative quantification of MB at 665 nm. Data were presented as mean \pm SD ($n = 3$ for each group). (j) The UV-vis absorption spectra of MB degradation in HGMP NPs solutions containing GSH (4 mM) and H₂O₂ (1 mM) under different pH conditions, and their remaining quantification of MB at 665 nm. Data were presented as mean \pm SD ($n = 3$ for each group).

via acylamide condensation. Subsequently, the MnO₂ shell was coated *in situ* on the surface of the obtained HMON-GOx NPs. As demonstrated by the TEM images, HMON-GOx@MnO₂ nanoparticles (HGM NPs) showed a mesoporous structure with an average diameter of 69.07 ± 4.10 nm (Fig. 1a and Fig. S1). High-angle annular dark-field-scanning transmission electron microscopy-based element mapping images demonstrated that the MnO₂ was successfully coated on the surfaces of HMON (Fig. 1a). Based on the GSH-responsive MnO₂ shell and disulfide bonds in the structure of HMON, a time-dependent degradation of the HGMP NPs was found in the presence of GSH (Fig. S2). The zeta potential changes indicated the successful synthesis of as-prepared HGM NPs and PEGylation (Fig. 1b). The surface area of HGMP NPs based on the Brunauer-Emmett-Teller (BET) measurement was calculated to $40.43 \text{ m}^2 \text{ g}^{-1}$ and the pore diameter was mainly concentrated in ~ 1.9 nm (Fig. S3). The result of X-ray photoelectron spectroscopy (XPS) confirmed the presence of C (C 1s peak at 284.8 eV), O (O 1s peak at 532.13 eV), Si (Si 2p peak at 102.66 eV), S (S 2p peak

at 163.51 eV), and Mn (Mn 2p peak at 642.35 eV and 654 eV) on the surface of HGMP NPs (Fig. 1c and d). In addition, the X-ray powder diffraction (XRD) result revealed that the diffraction peaks of MnO₂ could be observed in the HGMP NPs, which matched with the standard pattern of MnO₂ (Fig. S4). The colloidal stability study of HGMP NPs revealed that the HGMP NPs exhibited satisfactory stability during 2 days in various physiological solutions (Pure water, PBS, RPMI-1640 and RPMI-1640 with 10% FBS) (Fig. S5).

To verify the GOx catalytic activity of the HGMP NPs, H₂O₂ generation was assessed. As shown in Fig. 1e, a time-dependent generation of H₂O₂ was found in HGMP NPs solution. In contrast, no obvious H₂O₂ generation was found in HMP NPs solution. These results indicated that GOx generated additional H₂O₂ by the oxidation of β -D-glucose. Additionally, gluconic acid was also tested according to a reported method via UV-vis absorption spectra (Fig. S6 and S7) [28]. A time-dependent generation of gluconic acid catalyzed by HGMP NPs with glucose was found at 450–700 nm (the characteristic absorption band of a red com-

ound hydroxamate- Fe^{3+} generated between the reaction of gluconic acid, hydroxylamine, and FeCl_3). In contrast, no characteristic absorption band was found in PEGylated HMON@ MnO_2 nanoparticles (HMP NPs) solution containing glucose, indicating the catalytic activity of HGMP NPs on glucose oxidation.

HGMP NPs were designed as a nano ferroptosis inducer, due to its favorable GSH-depletion properties and manganese ion (Mn^{2+})-mediated Fenton-like reaction. As shown in Fig. 1f, the GSH content decreased in the HMP NPs solution in comparison with the pure water. This was due to the reaction between MnO_2 and GSH. Besides, the HGMP NPs depleted more GSH than the HMP NPs at the same Mn concentration. The GOx generated H_2O_2 by the oxidation of glucose. Subsequently, the H_2O_2 reacted with Mn^{2+} (product of reaction with GSH and MnO_2) to produce ROS, which was scavenged by GSH consumption. The GSH-responsive ROS-generating efficacy of HGMP NPs was evaluated using methylene blue as a ROS indicator. Firstly, the Fenton-like reaction performance of HMP NPs was examined. A dose-dependent tendency was found between the GSH concentration and the generation of ROS. As shown in Fig. 1g, the absorption peak of MB declined in the presence of H_2O_2 and GSH, caused by the GSH-activated Mn^{2+} released from the MnO_2 shell for the Fenton-like reaction. The optimum concentration range of GSH for MB degradation was wider (from 0 mM to 4 mM) than that previously reported for MnO_2 -coated mesoporous silica nanoparticles (MS@ MnO_2 NPs) (0 mM to 1 mM) [21]. This phenomenon was attributed to the extra GSH consumption mediated by the disulfide bond in the HMON core, avoiding the scavenging of ROS by GSH in a wider range. Moreover, the ·OH generation ability of HGMP NPs was measured by ESR analysis. The result revealed that the ·OH generation ability of HMP NPs via Mn^{2+} -mediated Fenton-like reaction could be well inherited by the HGMP NPs (Fig. 1h).

As verified above, HGMP NPs catalyzed the oxidation of glucose and produced H_2O_2 , which was correlated with the level of Fenton-like reaction generated ROS (Fig. S8a and b). Also, the HGMP NPs generated more ROS than the HMP NPs at the same Mn concentration in the presence of glucose (Fig. 1i). In addition, the absorption peak of MB decreased along with the decrease in pH value (from 7.4 to 6.5), suggesting that decreasing pH value could be an efficient way of promoting ROS generation (Fig. 1j). All these results indicated that HGMP NPs possessed a strong ability to induce the Fenton reaction in the tumor microenvironment (TME, mild acidity, high GSH and H_2O_2 concentration) [29,30].

3.2. PPI enhanced ferroptosis induction by decreasing cytoplasm pH value

Encouraged by the ability of both GSH depletion and ROS generation of HGMP NPs, the *in vitro* cytotoxicity of different NPs was further studied by the CCK-8 assay. Firstly, the cytotoxicity of HMP NPs in MC3T3-E1 normal cells and 4T1 tumor cells was evaluated. As shown in Fig. 2a, the viability of MC3T3-E1 cells was higher than 70% even at a high concentration of HMP NPs ([Mn]: 4.5 $\mu\text{g mL}^{-1}$) for 24 h. Moreover, the viability of 4T1 cells gradually declined with increased Mn concentration due to the high concentration of GSH and H_2O_2 in the TME, suggesting that HMP NPs could be a promising TME-responsive antitumor agent. Subsequently, it was assumed that GOx loading might further improve the tumor cell killing effect of HMP NPs, as GOx catalyzes the oxidation of glucose to generate H_2O_2 to enhance the Fenton reaction effect. As expected, 4T1 cells incubated with HGMP NPs showed lower cell viability than the HMP NPs groups at the same Mn concentration (Fig. 2b). Furthermore, the synergistic treatment of HGMP NPs and PPI was investigated. Although PPI alone showed no obvious toxicity in 4T1 cells at a concentration less than 25 $\mu\text{g mL}^{-1}$ (Fig. S9), the cytotoxicity of HGMP NPs was markedly increased, with cy-

totoxicity of 77% at the Mn concentration of 4.5 $\mu\text{g mL}^{-1}$ in PPI pretreated 4T1 cells. In comparison, cell death rate in the HMP group and HGMP group was 56% and 67% at the same Mn concentration, respectively (Fig. 2b). To evaluate *in vitro* uptake, HGMP NPs were modified with FITC and the fluorescent intensity in 4T1 cells was analyzed by flow cytometry. As shown in Fig. S10, a time-dependent increase of the uptake of HGMP NPs was observed in 4T1 cells.

Although the CCK-8 assay confirmed that the PPI and GOx could efficiently reinforce the cytotoxicity of HMP NPs, the mechanism requires further investigation. It is presumed that PPI may enhance Fenton-like reaction-based ferroptosis induction by inhibiting V-H⁺-ATPases protein expression and switching cytoplasm pH level. Therefore, western blot analysis was used to explore the mechanism of PPI-mediated pH value decrease in tumor cells. It was found that the V-H⁺-ATPases protein expression was down-regulated at the PPI concentration of 25 $\mu\text{g mL}^{-1}$ (Figs. 2c and S11), suggesting that the decrease in pH value benefitted from inhibition of the expression of V-H⁺-ATPases protein and prevention of the outflow of cytoplasm H⁺. Subsequently, the fluorescence intensity of the pH fluorescent probe BCECF AM was attenuated by the decrease in pH value, and was applied to evaluate whether intracellular pH level could be influenced by the inhibition of V-H⁺-ATPases. 4T1 cells treated with PPI (25 $\mu\text{g mL}^{-1}$) showed much weaker green fluorescence than cells treated with PBS (Fig. S12a). The intracellular fluorescence intensity of BCECF AM was further quantified by flow cytometry analysis and the results were consistent with fluorescence images (Fig. S12b). Similarly, green fluorescence intensity gradually decreased in PPI pretreated cells incubated with HGMP NPs compared with that in the HMP NPs and HGMP NPs treatment groups (Fig. 2d). These results indicated that GOx-mediated oxidation of glucose produced gluconic acid and PPI inhibited the efflux of intracellular H⁺. The level of intracellular green fluorescence was further quantified by flow cytometry analysis and the results were consistent with the fluorescence images (Fig. 2e).

We then investigated whether PPI and GOx could reinforce cytotoxicity through enhanced ferroptosis induction. GSH depletion, GPX4 expression level and ROS generation in 4T1 cells were examined. As shown in Fig. S13, the content of intracellular GSH decreased in the HMP NPs group compared with that in the PBS group. Besides, 4T1 cells incubated with HGMP NPs showed lower GSH concentration than the HMP NPs group at the same Mn concentration. This can be attributed to the fact that HGMP NPs generate more ROS in tumor cells due to increased H_2O_2 mediated by GOx-catalyzed glucose oxidation, triggering extra GSH consumption to scavenging ROS. When PPI was added to the culture medium, the decreased cytoplasm pH enhanced the Fenton-like reaction effect, depleting more GSH to scavenge intracellular ROS. HGMP NPs treatment decreased the GPX4 expression level in 4T1 cells (Fig. S14), suggesting that HGMP NPs could down-regulate GPX4 expression through MnO_2 -induced GSH consumption. Subsequently, the H_2O_2 generation in 4T1 cells incubated with various nanomaterials was assessed (Fig. S15). The decrease of intracellular H_2O_2 was found in HMP NPs treated 4T1 cells owing to Mn^{2+} -mediated Fenton-like reaction. Intracellular H_2O_2 concentration increased in the HGMP NPs group in comparison with the HMP NPs group since GOx could oxidize glucose to generate additional H_2O_2 . Besides, PPI-induced decrease in cytoplasm pH, which promoted the Fenton-like reaction effect triggering more H_2O_2 consumption. Moreover, ROS generation in 4T1 cells was detected by the DCFH-DA probe. Green fluorescence of 4T1 cells became stronger in the HGMP NPs group in comparison with that in the HMP NPs group (Fig. 2f). This can be attributed to the fact that HGMP NPs induce more severe oxidative stress in tumor cells due to increased H_2O_2 mediated by GOx-catalyzed glucose oxidation. Additionally, HGMP

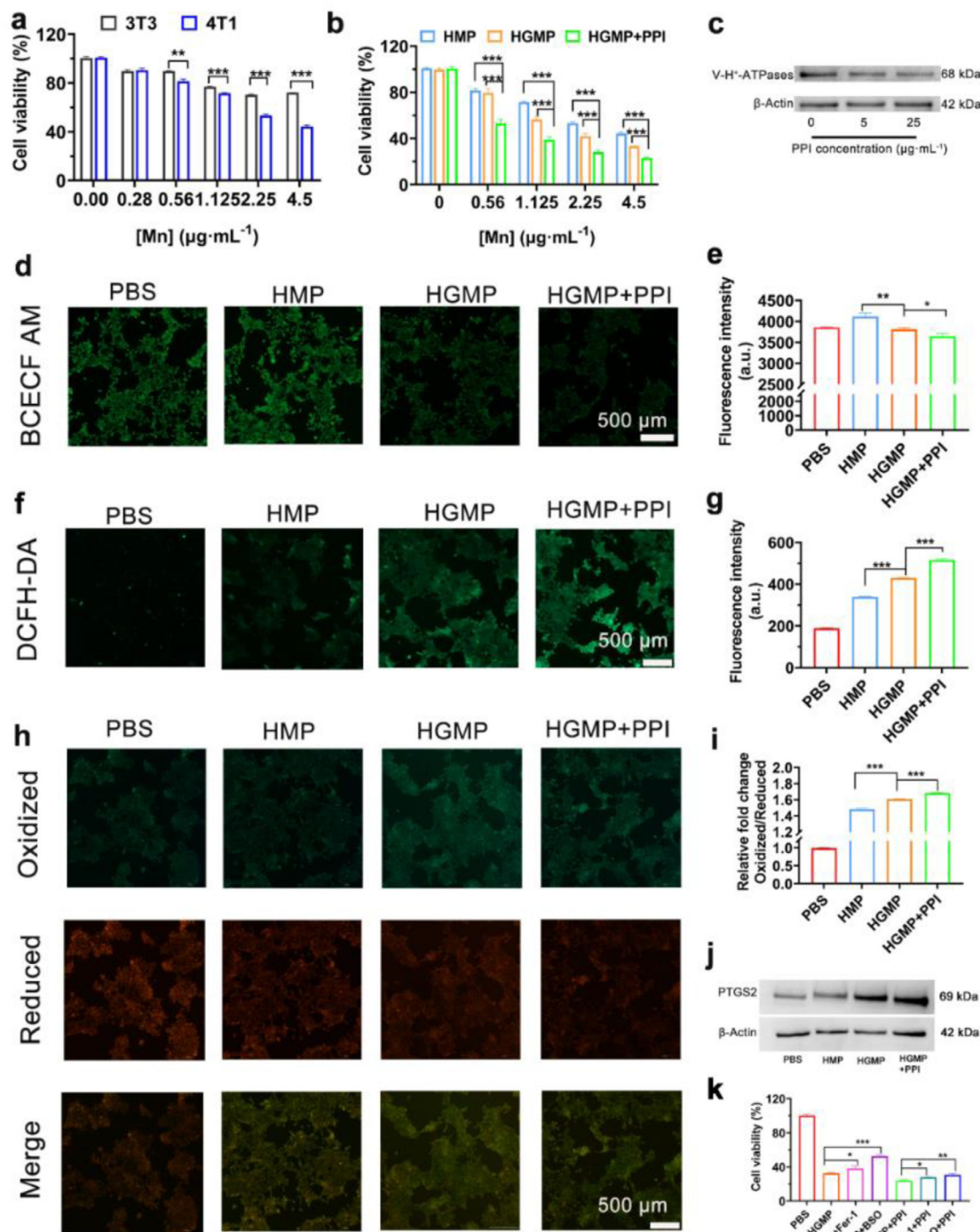


Fig. 2. *In vitro* cell experiments. (a) The cell viability of 3T3-E1 cells and 4T1 cells after incubation with HMP NPs for 24 h, respectively. Data were presented as mean \pm SD ($n = 3$ for each group). (b) Cell viability of 4T1 cells after varied treatments. Data were presented as mean \pm SD ($n = 3$ for each group). (c) Representative images of western blot analysis of V-H⁺-ATPases expression level in 4T1 cells after treatments with different concentrations of PPI for 24 h. (d) Representative images of 4T1 cells treated with varied samples and stained with BCECF AM probe (Scale bar = 500 μm), and (e) relative fluorescent intensity. Data were presented as mean \pm SD ($n = 3$ for each group). (f) Representative images of 4T1 cells exposed to varied treatments at the same Mn concentration and stained with DCFH-DA probe (Scale bar = 500 μm), and (g) relative fluorescent intensity. Data were presented as mean \pm SD ($n = 3$ for each group). (h) Representative images of 4T1 cells incubated with different samples at the same Mn concentration and stained with BODIPY 581/591 C11 (Scale bar = 500 μm), and (i) relative fluorescent intensity. Data were presented as mean \pm SD ($n = 3$ for each group). (j) Representative image of western blot analysis of PTGS2 expression level in 4T1 cells in different groups for 24 h. (k) Cell viability of 4T1 cells after varied treatments for 24 h. Data were presented as mean \pm SD ($n = 3$ for each group). * $P < 0.05$, ** $P < 0.01$, *** $P < 0.001$.

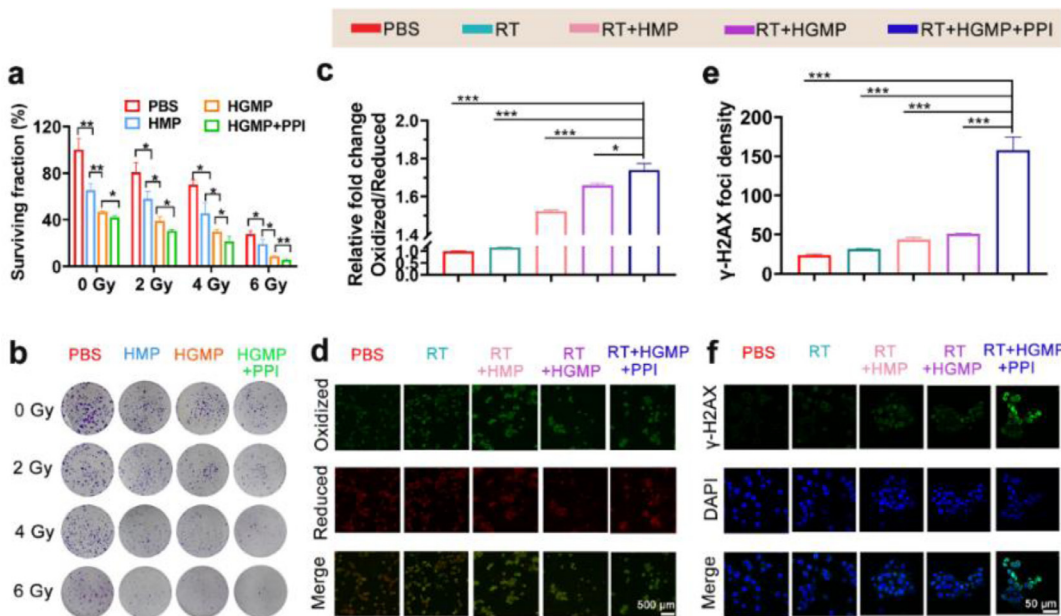


Fig. 3. *In vitro* PPI enhanced Ferroptosis inducing nanosystem-mediated radiotherapy. (a) Clonogenic survival fraction of 4T1 cells after various treatments and exposed with X-ray at different doses. Data were presented as mean \pm SD ($n = 3$ for each group). (b) Representative digital photos of clonogenic assay of 4T1 cells with different treatments from three biologically independent samples. (c) Relative fluorescent intensity and (d) representative images of 4T1 cells incubated with different samples followed by X-ray irradiation (4 Gy) and stained with BODIPY 581/591 C11 probe. Data were presented as mean \pm SD (Scale bar = 500 μ m; $n = 3$ for each group). (e) Quantitative analysis of γ -H2AX foci density for $n > 50$ cells and (f) representative immunofluorescence images of DNA damage marker γ -H2AX in 4T1 cells with different groups followed by X-ray irradiation (4 Gy). Green: γ -H2AX foci; Blue: cell nuclei. Data were presented as mean \pm SD (Scale bar = 50 μ m; $n = 3$ for each group). * $P < 0.05$, ** $P < 0.01$, *** $P < 0.001$.

NPs combined with PPI pretreatment further increased green fluorescence intensity of 4T1 cells (Fig. 2f), indicating that the decrease in cytoplasm pH promoted the Fenton-like reaction effect to generate more ROS. The level of ROS was quantified by flow cytometry analysis, which was consistent with the fluorescence images (Fig. 2g).

Furthermore, as the most important hallmark of ferroptosis [31], the accumulation of lipid peroxidation was evaluated by the lipid peroxidation fluorescent probe, BODIPY 581/591 C11. The increase in the ratio of Oxidized/Reduced lipid represents an elevated level of intracellular lipid peroxidation. As shown in Fig. 2h, green fluorescence of oxidized lipid in 4T1 cells was brighter in the HGMP group than in the HMP group, which further demonstrated the contribution of GOx in ferroptosis induction. Significant improvement in oxidized lipid was found when the cells were preincubated with PPI (Fig. 2h), indicating that the adjustment of cytoplasm pH value could also enhance ferroptosis induction. Flow cytometry also confirmed that synergistic treatment effectively induced lipid peroxidation (Fig. 2i). Moreover, PTGS2, one of the ferroptosis marker genes [32,33], was determined by western blot. As speculated, both HMP NPs and HGMP NPs treatment up-regulated PTGS2 expression level in 4T1 cells. More importantly, HGMP NPs combined with PPI pretreatment had a synergistic effect on inducing PTGS2 expression in 4T1 cells (Fig. 2j and Fig. S16). These results demonstrated that HGMP NPs have the potential to be a TME-activated ferroptosis induction agent, and PPI treatment could further strengthen the ability of ferroptosis induction.

To further confirm the cytotoxicity caused by ferroptosis induction, various ferroptosis inhibitors such as ferrostatin-1 (Fer-1, which can block lipid peroxidation) and L-BSO (which can inhibit glutamate-cysteine biosynthesis) were used to verify the mechanism of cell death induced by HGMP NPs [34,35]. Cell viability was increased in the HGMP NPs + Fer-1 group compared with HGMP NPs treated alone (Fig. 2k), which revealed that the dominant method of HGMP NPs-induced cell death was ferroptosis. Moreover, L-BSO + HGMP NPs significantly increased cell viability com-

pared with HGMP NPs alone or HGMP NPs + Fer-1 (Fig. 2k). As the synthesis of GSH was inhibited by L-BSO, the MnO₂ shell of HGMP NPs could not react with GSH to generate abundant Mn²⁺, and then trigger the Fenton-like reaction. In addition, PPI pretreatment increased the inhibition rate of HGMP NPs on 4T1 cells growth. Both Fer-1 and L-BSO pretreatment alleviated cell toxicity caused by PPI and HGMP NPs (Fig. 2k). All the above results demonstrated that the PPI and GOx promoted cytotoxicity caused by enhanced Fenton reaction for ferroptosis induction.

3.3. PPI boosted HGMP NPs-induced ferroptosis for RT sensitization

The contribution of PPI and GOx in reinforced ferroptosis induction has been verified, and whether this ferroptosis inducing nanosystem could be applied as a radiosensitizer was subsequently evaluated. As shown in the colony formation experiments (Fig. 3a and b), the survival fractions of tumor cells treated with RT (2 Gy) alone was 80.7% and decreased to 58% in the HMP NPs + RT (2 Gy) group, benefitting from ferroptosis induction of HMP NPs. The survival fraction in the HGMP NPs group was further decreased to 39% at a radiation dose of 2 Gy, due to the enhanced GOx catalyzed H₂O₂ supply. In addition, the survival fraction further decreased to 30.3% when the 4T1 cells were pretreated with PPI. To determine whether the increased chronic cytotoxicity was caused by ferroptosis induction, lipid peroxidation level in 4T1 cells in the different treatment groups was evaluated (Fig. 3c and d). It was shown that weak green fluorescence of oxidized lipid in 4T1 cells was observed in the RT (4 Gy) group, indicating that ionizing radiation can induce slight lipid peroxidation. Stronger green fluorescence was found in the HGMP NPs + RT (4 Gy) treatment group, which revealed that the NPs enhanced radiosensitization could be attributed to ferroptosis induction to some extent. The results of flow cytometry also demonstrated that GOx and PPI could further induce lipid peroxidation and improve RT efficacy. Additionally, γ -H2AX, a biomarker of double-strand DNA breaks, was also used to assess the degree of DNA in 4T1 cells. Confo-

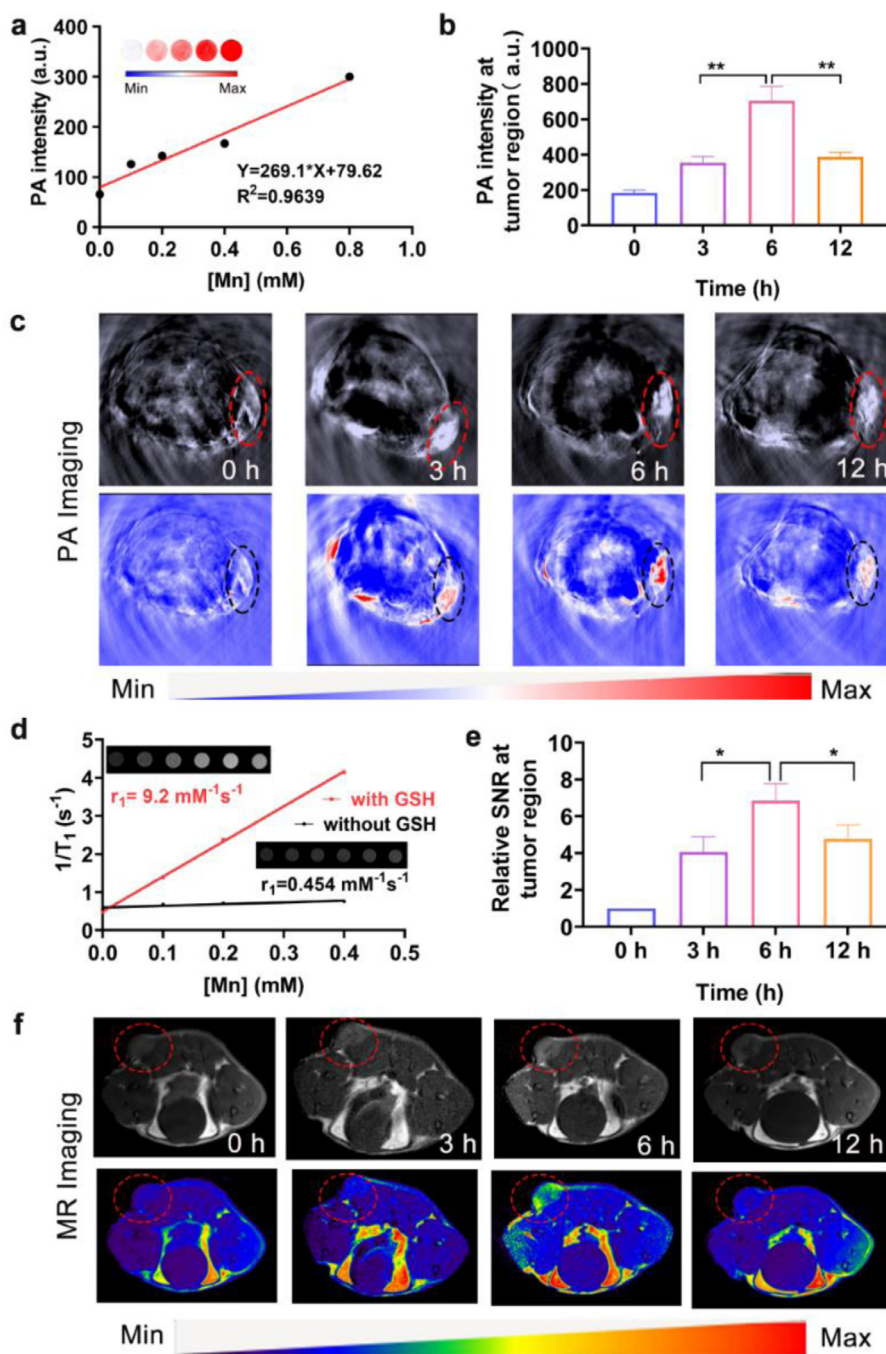


Fig. 4. *In vitro* and *in vivo* PA/MR imaging of HGMP NPs. (a) Linear correlation between average PA signal value and HGMP NPs solution at different Mn concentrations. (b) *In vivo* PA intensity at tumor region of 4T1 tumor-bearing mice before and after injection of HGMP NPs. Data were presented as mean \pm SD ($n = 3$ mice). (c) Representative PA images of 4T1 tumor-bearing mice before and after injection of HGMP NPs from three biologically independent samples. The red and black circle indicates tumor tissue. (d) The r_1 value of HGMP NPs solution with or without GSH (10 mM). (e) The calculated relative SNR at tumor region of 4T1 tumor-bearing mice before and after intravenous injection with HGMP NPs. Data were presented as mean \pm SD ($n = 3$ mice). (f) Representative T1-weighted MR images of 4T1 tumor-bearing mice before and after intravenous injection with HGMP NPs. * $P < 0.05$, ** $P < 0.01$.

cal laser scanning microscopy images showed that cells treated with PPI + HGMP and X-ray exposure showed strong DNA damage. In contrast, only mild DNA damage was detected in the PBS, RT, RT + HMP, and RT + HGMP treated groups compared with the other groups (Fig. 3e and f). Radiation dose-dependent cytotoxicity was found due to the as-prepared nanosystem as a radiosensitizer. These results indicated that PPI and GOx-boosted ferroptosis induction is effective in facilitating radiosensitization. Furthermore,

CRT exposure, the release of HMGB1 and ATP production as the hallmarks when cells are undergoing ICD were characterized [36]. Green fluorescence of CRT in 4T1 cells was observed in the HGMP NPs treatment group, and the X-ray irradiation could further enhance the CRT exposure (Fig. S18a and b). Besides, the green fluorescence of HMGB1 in 4T1 cells in the RT + HGMP NPs group was weaker than that in the PBS group and the HGMP NPs group (Fig. S18c and d). Consistently, evident ATP generation in 4T1 cells was

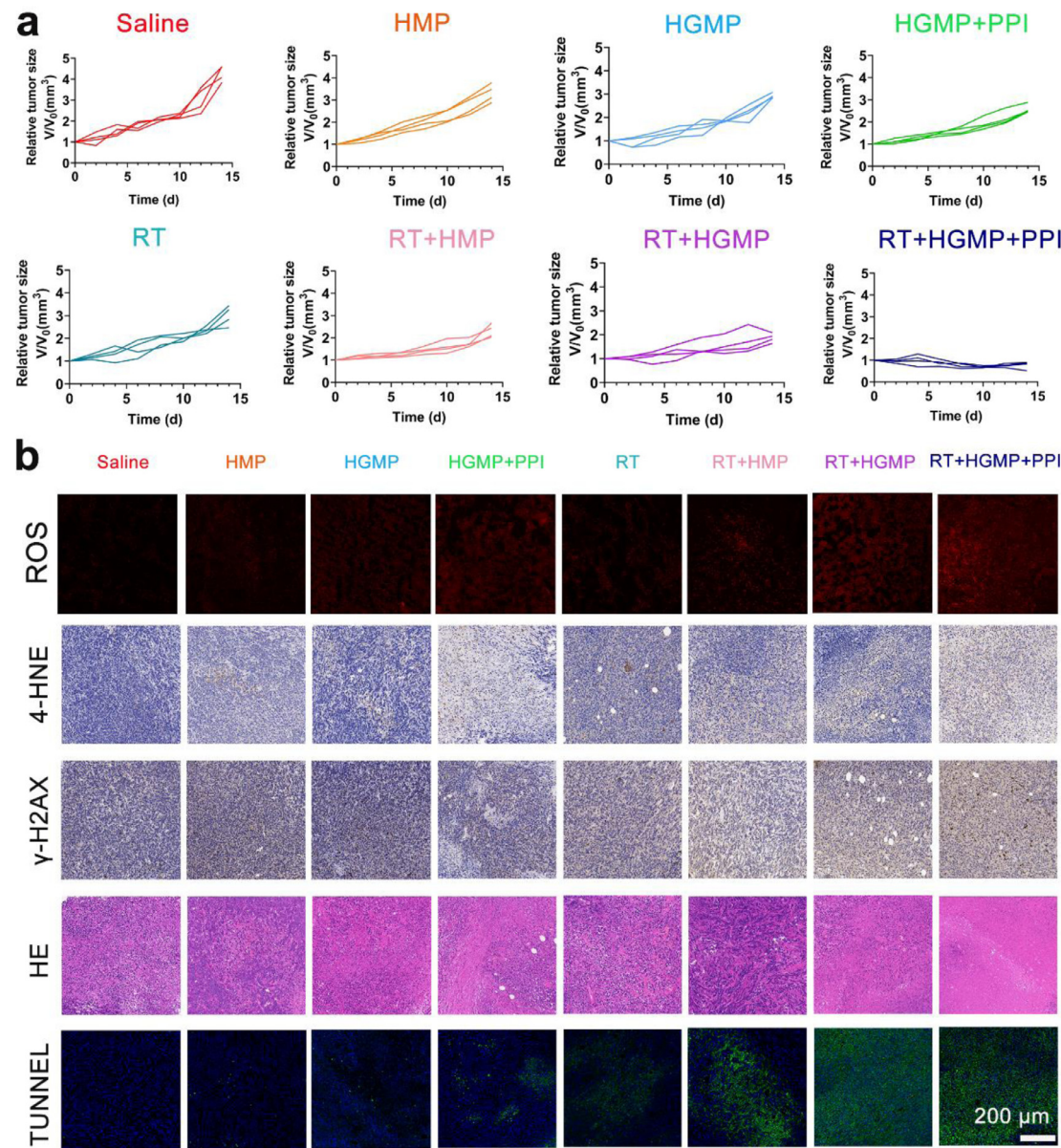


Fig. 5. Evaluation of the *in vivo* synergistic therapy. (a) Tumor growth curves of mice with different treatments over 14 days. Data were presented as mean \pm SD ($n = 4$ mice). (b) Representative pathological staining (ROS, 4-HNE antigen, γ -H2AX immunohistochemical assay, HE staining and TUNNEL) in tumor tissues (Scale bar = 200 μ m; $n = 3$ mice).

found in the HGMP NPs group and the RT + HGMP NPs group (Fig. S19). These results indicated that HGMP NPs induced ICD, which was further boosted by X-ray irradiation.

3.4. Monitoring the accumulation and reaction level of HGMP NPs at the tumor site by MR/PA bimodal imaging

Photoacoustic (PA) imaging is an emerging imaging modality, which combines optical excitation and acoustic detection, and may provide molecule-specific contrast and highly scalable spatial resolution [37,38]. It has been reported that MnO_2 based nanomaterials were promising candidates as PA imaging probes [39,40]. Herein, PA imaging was used to monitor the accumulation of HGMP NPs at the tumor site. The PA spectrum of HGMP NPs indicated that 680 nm was the optimal excitation wavelength (Fig. S20). The *in vitro* PA imaging demonstrated that the PA signal values of HGMP NPs were concentration-dependent (Fig. 4a). The *in vivo* PA imaging showed that the intratumoral PA signal reached a peak at 6 h

post intravenous injection of HGMP NPs (Fig. 4b and c), indicating that the HGMP NPs accumulated mostly in the tumor area at this time.

Furthermore, it was proved that the T1-weighted MRI enhancement relied on GSH-responsive Mn^{2+} release to monitor the Mn^{2+} mediated Fenton-like reaction. To evaluate the potential of HGMP NPs-mediated Mn^{2+} generation activated by GSH, the T1 relaxivity of HGMP NPs solutions before and after GSH treatment was determined using a 3.0 T MRI scanner (Fig. 4d). It was found that the relaxation rate (r_1 value) was stable in HGMP NPs solution without GSH, whereas the r_1 value increased by 20.8-fold when GSH was added. Additionally, T1-weighted MRI became brighter with increased Mn^{2+} concentration. This was attributed to the generation of Mn^{2+} by the reaction between MnO_2 and GSH. Based on the MRI contrast *in vitro*, T1-weighted MRI was performed to evaluate the contrast enhancement effect of HGMP NPs *in vivo*. *In vivo* T1-weighted MRI clearly showed that the T1 signal intensity in the tumor area gradually increased over time and the signal-to-noise

ratio (SNR) at the tumor area reached a peak at 6 h after injection (Fig. 4e and f). These results demonstrated that HGMP NPs were enriched in the tumor area at 6 h post-injection and generated amounts of Mn²⁺, which was consistent with *in vivo* PA imaging and further confirmed by the quantitative tumor accumulation analysis (Fig. S21). The PA/MR imaging indicated that HGMP NPs can be utilized as a promising contrast agent for molecular imaging, and 6 h post-injection of HGMP NPs could serve as an appropriate therapeutic time window for follow-up radiation therapy *in vivo*.

3.5. In vivo RT sensitization by PPI and GOx enhanced ferroptosis

Inspired by the good properties of PPI and GOx in the enhancement of ferroptosis induction and RT sensitization *in vitro*, the antitumor behavior in 4T1 tumor-bearing mice was assessed. Firstly, tumor tissue acidification induced by PPI was evaluated using a pH probe SNARF-1. The fluorescent intensity of SNARF-1 probe enhances with the decrease of pH value [10]. As shown in Fig. S22, strong fluorescence displayed in the tumor site at 6 h post-injection and then decreased over time, demonstrating that the pH in the tumor site decreased after using PPI. Subsequently, four groups of mice were injected intravenously with saline, HMP, HGMP, and HGMP + PPI, respectively. The other four groups of mice given the same treatments were then exposed to X-ray radiation at a dose of 6 Gy after injection for 6 h (the optimized time-point for both Mn-mediated ·OH generation and pH adjustment). Under ionizing radiation, the tumor volume was suppressed in the HMP NPs group compared with that in the saline group, indicating that HMP NPs as a ferroptosis inducing agent improved the efficacy of radiotherapy on solid tumors (Fig. 5a and Fig. S23). It was also found that more marked tumor growth suppression was observed in HGMP NPs-treated mice than in the HMP NPs group at the same dose of X-ray, which further confirmed the contribution of GOx in radiotherapy sensitization. Additionally, the inhibitory effect on tumor growth was significantly boosted in the PPI + HGMP NPs group under radiation, which demonstrated that PPI administration could facilitate ferroptosis induction for RT sensitization. No significant weight loss in any of the mice was observed during follow-up, which indicated the negligible systematic side effects of NPs-PPI + IR treatment (Fig. S24).

As reported previously [5], adaptive upregulation of GPX4 plays an important role in radioresistance. Considering the GSH consumption and GPX4 inhibitory ability of HGMP NPs proved *in vitro*, GPX4 antigen staining of tumor sections from mice injected intravenously with HGMP NPs was performed. The activity of GPX4 was indeed inhibited (Fig. S25). Dihydroethidium was used to evaluate the ROS generation in the tumor site. As shown in Fig. 5b and Fig. S26, increased ROS productivity was found in the sequence of HMP, HGMP and HFMP + PPI group. X-ray irradiation further enhanced the generation of intratumoral ROS. Furthermore, ferroptosis level in different groups was explored by 4-HNE antigen staining (Fig. 5b and S27a). Obvious staining under extra X-ray treatment was found in tumor tissue from mice treated with HMP NPs and HGMP NPs. In addition, the synergistic therapy of HGMP NPs + PPI with RT further increased 4-HNE staining in the majority of tumor cells, revealing that ferroptosis induction assisted by PPI administration plays a crucial role in tumor suppression. The γ-H2AX antigen staining, H&E and TUNEL staining were used to assess tumor morphology, apoptosis and DNA damage (Figs. 5b and S27b). When radiation was employed, the level of TUNEL staining, apoptosis and DNA damage were upregulated, suggesting that the enhanced efficacy of RT benefitted from both apoptosis and enhanced ferroptosis.

To evaluate the biosafety of HGMP NPs and PPI administration, serum samples from mice after injection of saline, HGMP NPs, PPI

or HGMP NPs + PPI were collected for biochemical analysis. Biochemical analysis of the blood-serum samples showed no obvious damage in kidney or liver (Fig. S28 and S30). In addition, H&E staining of the collected organs (heart, liver, spleen, lung, and kidney) also demonstrated that no obvious pathological changes were found in the major organs (Fig. S29 and S31). These findings revealed that the PPI administration and HGMP NPs did not have severe toxicity *in vivo*.

4. Conclusions

In conclusion, the TME-activated ferroptosis inducing nanoagent, PEGylated HMON-GOx@MnO₂ nanoparticles (HGMP NPs), were successfully constructed *in situ* by growing a MnO₂ shell on the surface of HMON-GOx NPs. In the tumor microenvironment, the MnO₂ shell of HGMP NPs was reduced *via* the reaction with intracellular GSH and generated Mn²⁺, triggering the Fenton-like reaction with endogenous H₂O₂ to produce ROS. The efficiency of the Fenton-like reaction was further boosted by H₂O₂ self-supply caused by GOx-mediated glucose oxidation. In addition, the generation of additional H⁺ originated from gluconic acid and the inhibitory effect of V-H⁺-ATPases activity induced by PPI could synergistically change the cytoplasm pH level and improve the efficacy of ferroptosis induction. In addition, the HGMP NPs could also be candidate contrast agents for PA imaging and GSH-responsive T1-weighted MRI to monitor the distribution and reaction state of HGMP NPs in the tumor area. Favorable antitumor effects were achieved both *in vitro* and *in vivo* benefitting from PPI and GOx enhanced ferroptosis induction for radiosensitization. Thus, HGMP NPs are a promising molecular imaging guided ferroptosis inducer to improve the efficacy of RT, and PPI administration can provide an efficient strategy to further enhance Fenton/Fenton-like reaction based ferroptosis induction for RT sensitization.

Declaration of competing interest

The authors declare that they have no competing interest.

Acknowledgments

We thank the entire staff of the Guangzhou Institute of Energy Conversion Chinese Academy of Sciences for TEM and HRTEM characterization.

Funding

This work was supported by the National Natural Science Foundation of China (Grant Numbers: 81871334, 81801764, 82072056, and 51937010); Guangdong Basic and Applied Basic Research Foundation (Grant Numbers: 2017A050506011, 2018030310343, 2020B1515020008, 2021A1515012542 and 2021A1515011882); Medical Scientific Research Foundation of Guangdong Province (Grant Number: A2018014), and the Pearl River Talented Young Scholar Program (Grant Number: 2017GC010282).

Data availability

All data are available from the authors upon reasonable request.

Supplementary materials

Supplementary material associated with this article can be found, in the online version, at doi:[10.1016/j.actbio.2023.03.011](https://doi.org/10.1016/j.actbio.2023.03.011).

References

- [1] T.A. Buchholz, Increasing the value of radiotherapy in breast cancer, *Lancet Oncol.* 22 (5) (2021) 572–573.
- [2] H. Li, M. Wang, B. Huang, S.W. Zhu, J.J. Zhou, D.R. Chen, R. Cui, M. Zhang, Z.J. Sun, Theranostic near-infrared-IIb emitting nanoprobes for promoting immunogenic radiotherapy and abscopal effects against cancer metastasis, *Nat. Commun.* 12 (1) (2021) 7149.
- [3] L.F. Ye, K.R. Chaudhary, F. Zandkarimi, A.D. Harken, C.J. Kinslow, P.S. Upadhyayula, A. Dovas, D.M. Higgins, H. Tan, Y. Zhang, M. Buonanno, T.J.C. Wang, T.K. Hei, J.N. Bruce, P.D. Canoll, S.K. Cheng, B.R. Stockwell, Radiation-Induced lipid peroxidation triggers ferroptosis and synergizes with ferroptosis inducers, *ACS Chem. Biol.* 15 (2) (2020) 469–484.
- [4] X. Lang, M.D. Green, W. Wang, J. Yu, J.E. Choi, L. Jiang, P. Liao, J. Zhou, Q. Zhang, A. Dow, A.L. Saripalli, I. Kryczek, S. Wei, W. Szeliga, L. Vatan, E.M. Stone, G. Georgiou, M. Cieslik, D.R. Wahl, M.A. MorganA.M. Chinnaiany, T.S. Lawrence, W. Zou (Eds.), Radiotherapy and immunotherapy promote tumoral lipid oxidation and ferroptosis via synergistic repression of SLC7A11, *Cancer Discov.* 9 (12) (2019) 1673–1685.
- [5] G. Lei, Y. Zhang, P. Koppula, X. Liu, J. Zhang, S.H. Lin, J.A. Ajani, Q. Xiao, Z. Liao, H. Wang, B. Gan, The role of ferroptosis in ionizing radiation-induced cell death and tumor suppression, *Cell Res.* 30 (2) (2020) 146–162.
- [6] Y. Liang, C. Peng, N. Su, Q. Li, S. Chen, D. Wu, B. Wu, Y. Gao, Z. Xu, Q. Dan, S. Zheng, B. Zhao, Y. Li, Tumor microenvironments self-activated cascade catalytic nanoscale metal organic frameworks as ferroptosis inducer for radiosensitization, *Chem. Eng. J.* 437 (2022) 135309.
- [7] M. Hou, K. Zhu, H. Hu, S. Zheng, Z. Wu, Y. Ren, B. Wu, L. Qi, D. Wu, Y. Xu, C. Yan, B. Zhao, Rapid synthesis of 'yolk-shell'-like nanosystem for MR molecular and chemo-radio sensitization, *J. Control Release* (2022).
- [8] X. Qian, J. Zhang, Z. Gu, Y. Chen, Nanocatalysts-augmented Fenton chemical reaction for nanocatalytic tumor therapy, *Biomaterials* 211 (2019) 1–13.
- [9] H. Deng, Z. Yang, X. Pang, C. Zhao, J. Tian, Z. Wang, X. Chen, Self-sufficient copper peroxide loaded pKa-tunable nanoparticles for lysosome-mediated chemodynamic therapy, *Nano Today* 42 (2022) 101337.
- [10] W. Bao, M. Liu, J. Meng, S. Liu, S. Wang, R. Jia, Y. Wang, G. Ma, W. Wei, Z. Tian, MOFs-based nanoagent enables dual mitochondrial damage in synergistic antitumor therapy via oxidative stress and calcium overload, *Nat. Commun.* 12 (1) (2021) 6399.
- [11] B.A. Webb, M. Chimenti, M.P. Jacobson, D.L. Barber, Dysregulated pH: a perfect storm for cancer progression, *Nat. Rev. Cancer* 11 (9) (2011) 671–677.
- [12] F. Chen, R. Kang, J. Liu, D. Tang, The V-ATPases in cancer and cell death, *Cancer Gene Ther.* (2022) 1–13.
- [13] M.P. Collins, M. Forgac, Regulation and function of V-ATPases in physiology and disease, *Biochim. Biophys. Acta Biomembr.* 1862 (12) (2020) 183341.
- [14] J.J. Lima, C.D. Thomas, J. Barbarino, Z. Desta, S.L. Van Driest, N. El Rouby, J.A. Johnson, L.H. Cavallari, V. Shakhnovich, D.L. Thacker, S.A. Scott, M. Schwab, C.R.S. Uppugunduri, C.M. Formea, J.P. Franciosi, K. Sangkuhl, A. Gaedigk, T.E. Klein, R.S. Gammal, T. Furuta, Clinical pharmacogenetics implementation consortium (CPIC) guideline for CYP2C19 and proton pump inhibitor dosing, *Clinic. Pharmacol. Therap.* 109 (6) (2021) 1417–1423.
- [15] L.Y. Yu, L.N. Sun, X.H. Zhang, Y.Q. Li, L. Yu, Z.Q. Yuan, L. Meng, H.W. Zhang, Y.Q. Wang, A review of the novel application and potential adverse effects of proton pump inhibitors, *Adv. Ther.* 34 (5) (2017) 1070–1086.
- [16] S. Bhattacharya, J. Khanam, P. Sarkar, T.K. Pal, A chemotherapeutic approach targeting the acidic tumor microenvironment: combination of a proton pump inhibitor and paclitaxel for statistically optimized nanotherapeutics, *RSC Adv.* 9 (1) (2019) 240–254.
- [17] M. Chen, J. Lu, W. Wei, Y. Lv, X. Zhang, Y. Yao, L. Wang, T. Ling, X. Zou, Effects of proton pump inhibitors on reversing multidrug resistance via downregulating V-ATPases/PI3K/Akt/mTOR/HIF-1 α signaling pathway through TSC1/2 complex and Rheb in human gastric adenocarcinoma cells in vitro and in vivo, *Oncotargets Ther.* 11 (2018) 6705–6722.
- [18] Y. Zhu, H. Shi, T. Li, J. Yu, Z. Guo, J. Cheng, Y. Liu, A dual functional nanoreactor for synergistic starvation and photodynamic therapy, *ACS Appl. Mater. Interfaces* 12 (16) (2020) 18309–18318.
- [19] M. Wang, M. Chang, C. Li, Q. Chen, Z. Hou, B. Xing, J. Lin, Tumor-microenvironment-activated reactive oxygen species amplifier for enzymatic cascade cancer starvation/chemodynamic /immunotherapy, *Adv. Mater.* 34 (4) (2022) 2106010.
- [20] B. Ding, P. Zheng, P. Ma, J. Lin, Manganese oxide nanomaterials: synthesis, properties, and theranostic applications, *Adv. Mater.* 32 (10) (2020) e1905823.
- [21] L.S. Lin, J. Song, L. Song, K. Ke, Y. Liu, Z. Zhou, Z. Shen, J. Li, Z. Yang, W. Tang, G. Niu, H.H. Yang, X. Chen, Simultaneous fenton-like ion delivery and glutathione depletion by MnO₂-based nanoagent to enhance chemodynamic therapy, *Angew. Chem. Int. Ed Engl.* 57 (18) (2018) 4902–4906.
- [22] Y. Zhang, R.V. Swanda, L. Nie, X. Liu, C. Wang, H. Lee, G. Lei, C. Mao, P. Koppula, W. Cheng, J. Zhang, Z. Xiao, L. Zhuang, B. Fang, J. Chen, S.-B. Qian, B. Gan, mTORC1 couples cyst(e)ine availability with GPX4 protein synthesis and ferroptosis regulation, *Nat. Commun.* 12 (1) (2021) 1589–1589.
- [23] B.R. Stockwell, A powerful cell-protection system prevents cell death by ferroptosis, *Nature* 575 (7784) (2019) 597–598.
- [24] W.S. Yang, R. SriRamaratnam, M.E. Welsch, K. Shimada, R. Skouta, V.S. Viswanathan, J.H. Cheah, P.A. Clemons, A.F. Shamji, C.B. Clish, L.M. Brown, A.W. Girotti, V.W. Cornish, S.L. Schreiber, B.R. Stockwell, Regulation of ferroptotic cancer cell death by GPX4, *Cell* 156 (1–2) (2014) 317–331.
- [25] X. Guan, L. Sun, Y. Shen, F. Jin, X. Bo, C. Zhu, X. Han, X. Li, Y. Chen, H. Xu, W. Yue, Nanoparticle-enhanced radiotherapy synergizes with PD-L1 blockade to limit post-surgical cancer recurrence and metastasis, *Nat. Commun.* 13 (1) (2022) 2834–2834.
- [26] J. Liu, X. Zhao, W. Nie, Y. Yang, C. Wu, W. Liu, K. Zhang, Z. Zhang, J. Shi, Tumor cell-activated "Sustainable ROS Generator" with homogeneous intratumoral distribution property for improved anti-tumor therapy, *Theranostics* 11 (1) (2021) 379–396.
- [27] W. Guo, Z. Chen, J. Chen, X. Feng, Y. Yang, H. Huang, Y. Liang, G. Shen, Y. Liang, C. Peng, Y. Li, G. Li, W. Huang, B. Zhao, Y. Hu, Biodegradable hollow mesoporous organosilica nanotheranostics (HMON) for multi-mode imaging and mild photo-therapeutic-induced mitochondrial damage on gastric cancer, *J. Nanobiotechnol.* 18 (1) (2020) 99.
- [28] C. Peng, Y. Liang, N. Su, S. Chen, Z. Yuan, Y. Chen, D. Wu, B. Wu, Y. Zhang, Z. Xu, S. Zheng, Y. Li, B. Zhao, Dual nanoenzymes loaded hollow mesoporous organonatural nanospheres for chemo-radio sensitization, *J. Control Release* 347 (2022) 369–378.
- [29] L.H. Fu, Y. Wan, C. Qi, J. He, C. Li, C. Yang, H. Xu, J. Lin, P. Huang, Nanocatalytic theranostics with glutathione depletion and enhanced reactive oxygen species generation for efficient cancer therapy, *Adv. Mater.* 33 (7) (2021) e2006892.
- [30] J. Xin, C. Deng, O. Aras, M. Zhou, C. Wu, F. An, Chemodynamic nanomaterials for cancer theranostics, *J. Nanobiotechnol.* 19 (1) (2021) 192–192.
- [31] Scott J. Dixon, Kathryn M. Lemberg, Michael R. Lamprecht, R. Skouta, Eleina M. Zaitsev, Caroline E. Gleason, Darpan N. Patel, Andras J. Bauer, Alexandra M. Cantley, Wan S. Yang, B. Morrison, Brent R. Stockwell, Ferroptosis: an iron-dependent form of nonapoptotic cell death, *Cell* 149 (5) (2012) 1060–1072.
- [32] D. Tang, X. Chen, R. Kang, G. Kroemer, Ferroptosis: molecular mechanisms and health implications, *Cell Res.* 31 (2) (2021) 107–125.
- [33] B. Stockwell, J. Friedmann Angelis, H. Bayir, A. Bush, M. Conrad, S. Dixon, S. Fulda, S. Gascón, S. Hatzios, V. Kagan, K. Noel, X. Jiang, A. Linkermann, M. Murphy, M. Overholtzer, A. Oyagi, G. Pagnussat, J. Park, Q. Ran, C. Rosenfeld, K. Salnikow, D. Tang, F. Torti, S. Torti, S. Toyokuni, K. Woerpel, D. Zhang, Ferroptosis: a regulated cell death nexus linking metabolism, redox biology, and disease, *Cell* 171 (2) (2017) 273–285.
- [34] G. Miotti, M. Rossetto, M.L. Di Paolo, L. Orian, R. Venerando, A. Roveri, A.-M. Vučković, V. Bosello Travaini, M. Zaccarin, L. Zennaro, M. Maiorino, S. Toppo, F. Ursini, G. Cozza, Insight into the mechanism of ferroptosis inhibition by ferrostatin-1, *Redox Biol.* 28 (2020) 101328–101328.
- [35] Y. Sun, Y. Zheng, C. Wang, Y. Liu, Glutathione depletion induces ferroptosis, autophagy, and premature cell senescence in retinal pigment epithelial cells, *Cell Death. Dis.* 9 (7) (2018) 753–753.
- [36] K. Zhu, Z. Wu, Q. Li, M. Hou, H. Hu, S. Zheng, L. Qi, Y. Xu, C. Yan, B. Zhao, Immune microenvironment-reshaping Au@Bi₂Te₃ nanoparticles for spectral computed tomography/photoacoustic imaging-guided synergistic photo/radio/immunotherapy, *Nano Res.* 16 (1) (2023) 771–781.
- [37] C. He, J. Zhu, H. Zhang, R. Qiao, R. Zhang, Photoacoustic imaging probes for theranostic applications, *Biosensors* 12 (11) (2022).
- [38] C. Liu, X. Zheng, T. Dai, H. Wang, X. Chen, B. Chen, T. Sun, F. Wang, S. Chu, J. Rao, Reversibly photoswitching upconversion nanoparticles for super-sensitive photoacoustic molecular imaging, *Angew. Chem. Int. Ed Engl.* 61 (19) (2022) e202116802.
- [39] C. Liu, D. Wang, Y. Zhan, L. Yan, Q. Lu, M.Y.Z. Chang, J. Luo, L. Wang, D. Du, Y. Lin, J. Xia, Y. Wu, Switchable photoacoustic imaging of glutathione using MnO₂ nanotubes for cancer diagnosis, *ACS Appl. Mater. Interfaces* 10 (51) (2018) 44231–44239.
- [40] M. Luo, Y. Lv, X. Luo, Q. Ren, Z. Sun, T. Li, A. Wang, Y. Liu, C. Yang, X. Li, Developing smart nanoparticles responsive to the tumor micro-environment for enhanced synergism of thermo-chemotherapy with PA/MR bimodal imaging, *Front. Bioeng. Biotechnol.* 10 (2022) 799610.